

Enhanced Mass-to-Light Ratios in UCDs through Tidal Interaction with the Centre of the Host Galaxy

M. Fellhauer^{1,2,3}  and P. Kroupa^{1,2} 

¹ Argelander Institute for Astronomy, University Bonn, Auf dem Hugel 71, 53121 Bonn

² The Rhine Stellar-Dynamical Network

³ Institute of Astronomy, University of Cambridge, Madingley Road, Cambridge CB3 0HA

20 March 2024

ABSTRACT

A recent study of ultra-compact dwarf galaxies (UCDs) in the Virgo cluster revealed that some of them show faint envelopes and have measured mass-to-light ratios of 5 and larger, which can not be explained by simple population synthesis models. It is believed that this proves that some of the UCDs must possess a dark matter halo and may therefore be stripped nuclei of dwarf ellipticals rather than merged star cluster complexes.

Using an efficient N-body method we investigate if a close passage of a UCD through the central region of the host galaxy is able to enhance the measured mass-to-light ratio by tidal forces leaving the satellite slightly out of virial equilibrium and thereby leading to an overestimation of its virial mass.

We find this to be possible and discuss the general problem of measuring dynamical masses for objects that are probably interacting with their hosts.

Key words: galaxies: dwarfs – galaxies: interactions – galaxies: kinematics and dynamics – methods: N-body simulations

1 INTRODUCTION

Hasegan et al. (2005) investigated ultra-compact dwarf galaxies (UCDs) around M87, the central galaxy of the Virgo cluster. By measuring the surface brightness profiles and assessing the projected velocity dispersion of the objects they concluded that some UCDs of their sample have mass-to-light ratios of the order 5–9. Furthermore, they find that some of the UCDs show faint envelopes. This supports the notion that these UCDs may be stripped nuclei of dwarf ellipticals.

UCDs were first discovered by Hilker (1998); Hilker, Infante & Richtler (1999) during a study of globular clusters and dwarf galaxies around the central galaxy in the Fornax cluster. These objects are compact with effective radii of about 15–25 pc and a hundred to several hundred pc in extension, and they are massive with masses of a few 10^6 up to a few $10^7 M_{\odot}$.

There are several theories about the origin of UCDs: (I) They could be the most luminous end of the distribution function of very massive globular clusters (Hilker et al. 1999; Mieske et al. 2002; Dirsch et al. 2003). (II) They could be the remnants of stripped dwarf ellipticals (Bekki, Couch & Drinkwater 2001; Bekki et al. 2003; De Propris et al. 2005). In this ‘threshing’ scenario a nucleated dwarf elliptical loses its envelope and most of its dark matter content due to tidal interaction with the host galaxy, such

that only the ‘naked’ nucleus remains. (III) They could be amalgamated young massive star clusters formed in a star cluster complex during the star-burst caused by the tidal perturbation and possible disruption of a gas-rich galaxy (Fellhauer & Kroupa 2002, 2005). This scenario is well-established theoretically and was first proposed by Kroupa (1998). It must have been profusively active during the early hierarchical structure formation epoch when gas-rich substructures merged to the present-day major galaxies.

It is still under debate whether the UCDs, which fill the gap between globular clusters and dwarf galaxies, follow the fundamental plane (effective radius / velocity dispersion – total luminosity) relation for globular clusters or for dwarf galaxies (Hasegan et al. 2005; Evstigneeva, Gregg & Drinkwater 2005). While, in the M_V – σ -plane (see e.g. Hasegan et al. 2005, their Fig. 7), they lie closer to the globular clusters, their relation seems to rather follow the one of dwarf galaxies. Furthermore they occupy exactly the space between dwarf ellipticals and their nuclei. This seems to point to formation theory (II). But the surface brightness profiles of the bright UCDs in Fornax are much more extended (i.e. larger effective radii) compared with nuclei of dEs (De Propris et al. 2005).

On the other hand, Maraston et al. (2004) found an intermediate age object (W3, age 300–500 Myr) in the merger remnant galaxy NGC 7252. The mass ($M = 8 \cdot 10^6 M_{\odot}$), size ($r_e = 17.5$ pc, and velocity dispersion of 45 km s^{-1}) strongly suggest this object to be a UCD rather than a globular cluster. The age of this object, which corresponds to the time elapsed since the major interaction, unambiguously shows that this object can not be

[?] madf@ast.cam.ac.uk

y pavel@astro.uni-bonn.de

Table 1. Table of our initial model parameters. The columns denote the initial mass of our model ($M_{p1} = M_{in1}$), the scale length (Plummer radius, R_{p1} ; analytical & measured as described in Sect. 3), the characteristic crossing time (T_{cr}), the central projected (line-of-sight) velocity dispersion (σ_{p1} ; analytical & measured as described in Sect. 3), and the scaling factor (A) to compute the virial mass (see Eq. 11).

Mass [M_{\odot}]	R_{p1} [pc]	measured	T_{cr} [Myr]	σ_{p1} [km s^{-1}]	measured	A
10^7	25	23:7	3:69	15:92	16:20	1608
10^7	50	46:6	10:43	11:25	11:71	1565
10^7	100	94:6	29:50	7:96	8:43	1487
10^7	250	221:0	116:61	5:03	6:30	1140
10^8	25	25:2	1:17	50:33	50:2	1573
10^8	50	47:4	3:30	35:59	36:8	1558
10^8	100	92:8	9:33	25:16	26:9	1489
10^8	250	213:0	36:88	15:92	19:91	1184

a stripped nucleus of a dwarf elliptical. A dwarf elliptical can not be stripped in a time interval of only 500 Myr. Fellhauer & Kroupa (2005) showed that W3 could be the merger object of a massive star cluster complex which was formed during the interaction. The subsequent merging of star clusters forms an object with properties similar to those of W3. The evolution of the simulated super cluster shows that it transforms into a UCD such as those found in Fornax (Hilker et al. 1999; Phillipps et al. 2001), Abell 1689 (Mieske et al. 2004), and Virgo (Hasegan et al. 2005; Evstigneeva et al. 2005). Moreover, Fellhauer & Kroupa (2005) showed that, due to its high mass, the object was able to retain an envelope of bound stars which initially were expelled from the individual clusters during the merger process. Thus, an envelope around a UCD is not a proof of its cosmological origin as a dwarf elliptical. Still the puzzle of high mass-to-light ratios of some of the UCDs in Virgo remains. These mass-to-light ratios (5–9) are found for the UCDs lying closest to the host galaxy. This suggests that deviations from virial equilibrium may play a role.

The reasoning is that dwarf galaxies are on radial rather than circular orbits, if the UCDs formed as star-cluster complexes during the merging of major gas-rich substructures. This allows the satellites to pass close to the galactic centre. Tidal forces in the central region of the host galaxy are rather strong. Hence, the dwarf object loses stars and subsequently departs from virial equilibrium. Some of the lost stars (stars which are no longer bound to the object) do not immediately leave the object or its vicinity but disperse slowly along the orbit. Thus, a line-of-sight velocity dispersion measurement may be contaminated by these unbound stars which inflate the velocity dispersion. Furthermore, the gravitational shock of the central passage leads to an expansion of the dwarf galaxy which is later reversed again. But still this expansion through tidal heating may result in a measurable increase of the core radius once the dwarf object is again outside the host galaxy. Both of these effects may lead to an overestimation of the measured dynamical mass resulting in a higher mass-to-light ratio. These effects are not new to the astronomical community and are studied intensively by various authors (e.g. Kroupa 1997) for dwarf spheroidals, (Mayer et al. 2001, 2002) for dwarf discs and dwarf spheroidals or (Bekki et al. 2003) for dwarf ellipticals). With this paper we want to extend these studies onto massive (compared to globular clusters) and compact (compared to other dwarf galaxies) objects like UCDs.

It is definitely clear that these effects must be very strong if an object comes close to the galactic centre. But on the other hand these very close passages may be highly unlikely. By means of nu-

merical simulations we intend to find out which sets of orbits allow an enhanced mass-to-light ratio, i.e. how close the UCD has to approach to the centre of its host galaxy, for which we choose the parameters of M87 to account for the UCDs with high mass-to-light ratios found around the central galaxy of Virgo.

2 SETUP

We model the parent galaxy as an analytical potential because on one single passage dynamical friction for a dwarf galaxy of mass $M \approx 6 \cdot 10^8 M_{\odot}$ affects the orbit to at most 2–3 per cent, estimated using Chandrasekhar’s formula (Chandrasekhar 1943) as described in Portegies Zwart & McMillan (2002). We also look for only one central passage because unbound stars disperse along the orbit and are lost at subsequent passages. Some of them might still be around the object after the second or third central passage but definitely not for dozens of orbits.

As a model for the analytical potential we choose the parameters for M87, the central galaxy in the Virgo cluster, consisting of a NFW-profile for the dark halo, a Hernquist profile (H) for the visible matter (stars) and a central super-massive black hole (BH) (McLaughlin 1999; Vesperini et al. 2003; Di Matteo et al. 2003). The density profile of the host galaxy is

$$\begin{aligned} \rho_{tot}(r) &= \rho_{NFW}(r) + \rho_H(r) \\ &= \frac{\rho_{NFW} \cdot r_{s,NFW}}{r \left(1 + \frac{r}{r_{s,NFW}}\right)^2} + \frac{M_H \cdot r_{s,H}}{2 \cdot r \cdot (r_{s,H} + r)^3}; \end{aligned} \quad (1)$$

with the following parameters,

$$\rho_{NFW} = 3.17 \cdot 10^4 M_{\odot} \text{pc}^{-3}; \quad (2)$$

$$r_{s,NFW} = 560 \text{ kpc}; \quad (3)$$

$$M_H = 8.1 \cdot 10^7 M_{\odot}; \quad (4)$$

$$r_{s,H} = 5.1 \text{ kpc}; \quad (5)$$

$$M_{BH} = 3 \cdot 10^9 M_{\odot}; \quad (6)$$

The above parameters denote from top to bottom the characteristic density and the scale-length of the NFW-profile, the total mass and the scale-length of the Hernquist-profile and finally the mass of the central super-massive black hole.

We model the UCD as a Plummer-sphere (Plummer 1911) in the numerical realisation described by Aarseth, Henon & Wielen

Table 2. List of minimum distances and the corresponding tangential velocities at the start of the simulation.

D_{min} [pc]	v_{tan} [km s ⁻¹]
0	0.0
50	6.0
100	10.9
150	15.9
250	25.4
500	48.1
1000	89.3
1500	126.0
2000	158.9

(1974),

$$\rho_{\text{pl}}(r) = \frac{3M_{\text{pl}}}{4R_{\text{pl}}^3} \left(1 + \frac{r^2}{R_{\text{pl}}^2} \right)^{-5/2}; \quad (7)$$

with varying scale-lengths, R_{pl} , and initial masses, M_{pl} , because De Propriis et al. (2005) found a Plummer-profile to fit four out of five UCDs in the Fornax cluster quite well. Furthermore, the Plummer model is analytically simple and the Plummer radius is not only the scale-length of the model but also its half-light (the projected radius from within which half of the light of the object is emitted).

The masses of UCDs range between several million M_{\odot} up to several tens of millions. So we choose for our models 10^7 and $10^8 M_{\odot}$ as initial masses ($M_{\text{pl}} = M_{\text{in,i}}$). We vary the initial scale-length of our models to be $R_{\text{pl}} = 25, 50, 100$ and 250 pc to determine the influence of the concentration of the objects. The cut-off radius (R_{lim} ; the radius where we truncate the Plummer distribution of our object) of all our models was kept constant at 500 pc which is larger than the initial tidal radius. A detailed list of our model parameters can be found in Table 1. The Plummer spheres are modelled using 10^6 particles. The object is set-up and integrated in isolation until equilibrium, as measured by the constancy of the 90 % Lagrangian radius, is reached (Kroupa 1997).

The UCD model is then placed at a distance of 10 kpc to the centre of the host galaxy with no radial velocity. This means that the effect of the central passage is the most harmful possible because it is the slowest possible. The faster the passage would be (if the satellite was to start further out) the less tidal influence the central passage would have. No UCD is found closer than 10 kpc from the centre of its host and therefore it acts as a minimum apogalacticon, which has the strongest tidal effect possible. To vary the minimum distance (perigalacticon) we give our models different tangential velocities which are listed in Tab. 2. We assume the problem to be spherically symmetric, so we are able to place the trajectory of our model in the x-y-plane of our simulation area without restricting the problem.

We use the particle-mesh code SUPERBOX to carry out the simulations. SUPERBOX has high-resolution sub-grids which stay focused on the core of the dwarf object while it is moving through the host galaxy. The resolution of the innermost grid containing the core is 3 pc. For a detailed description of the code see Fellhauer et al. (2000).

3 RESULTS

We carried out a parameter survey of 76 simulations covering different dwarf galaxy objects and different orbits. The parameter range is shown in Tables 1 and 2. For each parameter set one simulation over two central passages is carried out. For the determination of our results we look at the satellite when it reaches apogalacticon again after the first central passage.

3.1 The analytical method

The surface density profile of the satellite is fitted by a Plummer profile of the form

$$\rho(r) = \rho_0 \left(1 + \frac{r^2}{R_{\text{pl}}^2} \right)^{-2}; \quad (8)$$

by applying a non-linear least-squares Marquardt-Levenberg algorithm. From this procedure we take the fitted Plummer radius for our determination of the virial mass. It can be shown that the Plummer radius exactly coincides with the half-light (projected half-mass) radius of a Plummer sphere.

Furthermore we determine the line-of-sight velocity dispersion profile. In cases where it is possible, i.e. the profile is not too contaminated by unbound stars, we again fit the Plummer profile for the line-of-sight velocity dispersion,

$$\sigma_p(r) = \sigma_{0,p} \left(1 + \frac{r^2}{R_{\text{pl}}^2} \right)^{-1/4}; \quad (9)$$

The projected velocity dispersion, as well as the surface density, is measured along all three Cartesian coordinates in logarithmically spaced, concentric rings centred on the object. For the measurement all stars within a certain distance R_{max} in front and behind the centre of the object are taken into account. The procedure is done along all three Cartesian axes and we take the arithmetic mean value (i.e. a mean profile), because we do not know which orientation our objects have with respect to the observer. Therefore effects may be very strong measuring along the trajectory of the object but almost not visible in the perpendicular direction. Any random direction is likely to yield an intermediate result.

For the surface density we always fit a Plummer profile even if the object is completely destroyed and does not follow a Plummer distribution at all. But in most of our models the remaining object is still fairly well represented by a Plummer profile even if it is on the way to complete destruction. In cases where we are not able to fit the velocity dispersion profile with a Plummer profile (see e.g. first panel of Fig. 3) we take an average of all measured line-of-sight velocity dispersion values within the innermost 10 pc in projected radius to determine the central line-of-sight velocity dispersion.

We now determine the virial mass taking the formula from Hasegan et al. (2005) which is based on the theoretical work of King (1966),

$$M_{\text{vir}} = \frac{9}{2} \frac{R_c}{G} \frac{\sigma_{0,p}^2}{p}; \quad (10)$$

where R_c is the core radius and $\sigma_{0,p}$ is the central value of the projected velocity dispersion. The parameters $\sigma_{0,p}$, R_c , and p are dependent on the kind of King model one wants to fit. Because we are using Plummer spheres we accumulate these parameters together with the constants into one single parameter A , which we determine for the isolated Plummer sphere before we start the simulation,

$$M_{\text{vir}} = A R_{\text{pl}} \frac{\sigma_{0,p}^2}{p}; \quad (11)$$

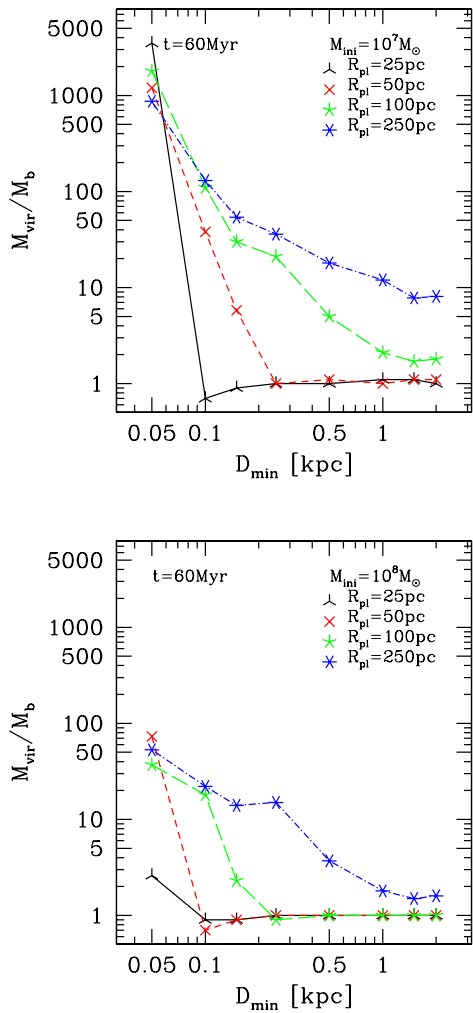


Figure 1. The ratio between virial and bound mass ($M_{\text{vir}}/M_{\text{b}}$) for our objects, measured at $t = 60$ Myr, the point where the object is again most distant to the centre of the host galaxy, against the closest distance from the centre of the host (D_{min}). First panel: Objects with initial mass of $10^7 M_{\odot}$. Second panel: Objects with initial mass of $10^8 M_{\odot}$. Tri-pointed stars (online: black) denote objects with initial Plummer radii of $R_{\text{pl}} = 25$ pc, crosses (online: red) have $R_{\text{pl}} = 50$ pc, five-pointed stars (online: green) have $R_{\text{pl}} = 100$ pc, and six-pointed stars (online: blue) $R_{\text{pl}} = 250$ pc.

where the values of the scaling factor A can be found in Table 1. As one can see these values are lower for higher masses and increase for larger scale-lengths. Nevertheless we use the same A determined for the isolated model for all final models stemming from this initial model, even if the mass-loss is significant. This may lead to a slight underestimation of the final virial mass.

On the other hand SUPERBOX calculates the number of bound particles (energy below zero) at each time-step. Therefore we know the real bound mass M_{b} .

With these two masses we can determine a virial-mass-to-bound-mass ratio ($M_{\text{vir}}/M_{\text{b}}$ or short M/M) which can then be multiplied by a 'normal' mass-to-light ratio for a population of stars with the determined age and metallicity and without dark matter to obtain the dynamically measured $M=L$ -ratio.

This M/M -ratio is plotted in Fig. 1, when the satellites have reached their apogalactica again. At this point the satellites are al-

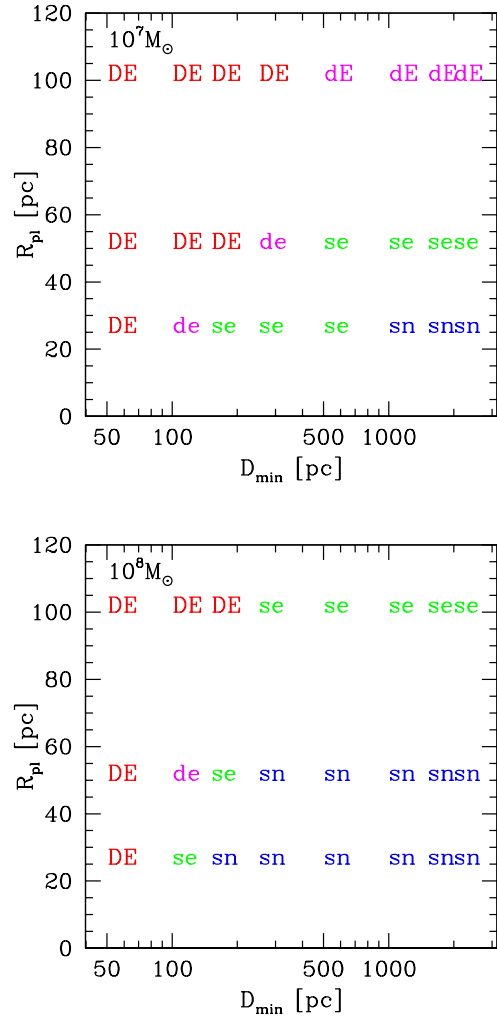


Figure 2. Parameter space of our simulations; Plotted are the Plummer radius of our models, R_{pl} , against the closest distance to the centre of the host galaxy, D_{min} . Capital D (online: red) denotes the satellite gets completely dissolved during the first passage. Small d (online: magenta) denotes satellites which do not survive the next central passage. Small s denotes satellites which survive and form bound objects even after the next central passage. Capital E marks simulations where the M/M -ratio is enhanced if the central values are directly measured. Small e marks simulations which only show enhanced M/M -ratios if the observational method is applied (see main text for explanation). Surviving satellites with enhanced M/M -ratios are plotted green online. Finally, n marks simulations which show no enhancement measured with either method (online: blue). First panel is for objects with initial mass of $10^7 M_{\odot}$, second panel for $10^8 M_{\odot}$.

most back to virial equilibrium again if they are not on the way to complete dissolution.

The results show clearly that only objects which are not compact and/or have a low mass can be influenced enough by one central passage to enhance the M/M to account for the high mass-to-light ratios found in UCDs. But these satellites will also not survive the next central passage or have not survived the first one at all.

The best representation of real UCDs is the model with an initial mass of $10^7 M_{\odot}$ and an initial Plummer radius of 25 pc. The results for this model are shown as tri-pointed stars in the first panel of Fig. 1 and the lowest line in the first panel of Fig. 2. The results

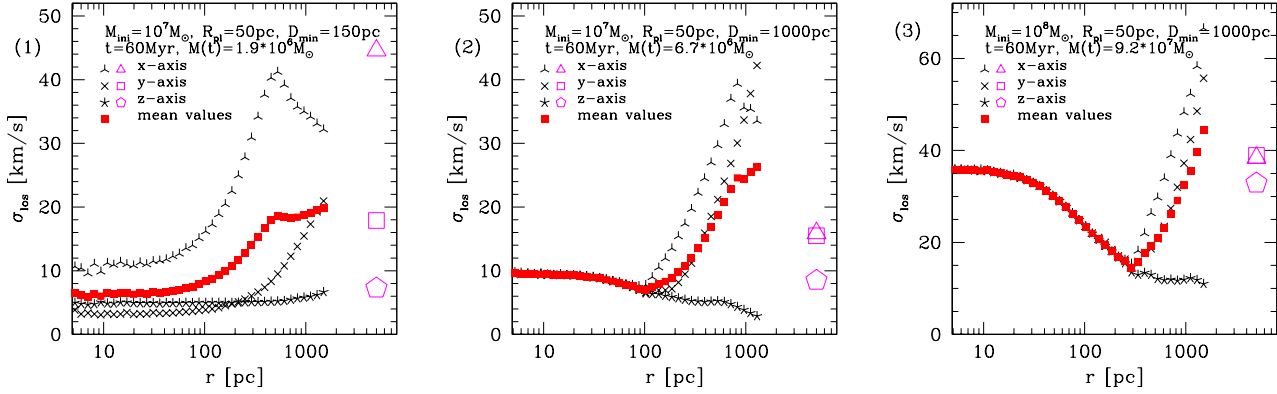


Figure 3. Line-of-sight velocity dispersion profiles and the Gaussian fit values for three of our satellites. Three-, four- and five pointed stars denote the line-of-sight velocity dispersion values measured in concentric rings around the satellite along the x-, y and z-axis, respectively. Filled squares (online: red) are the mean values of all directions. Open symbols (online: magenta) on the right denote the central line-of-sight velocity dispersion values derived with the observational method (see Fig. 5). First panel: This object gets completely dissolved and shows an enhancement of the velocity dispersion in either method. But this destroyed satellite can not account for the UCDs in Virgo (see Fig. 4). Second panel: Object which shows an enhancement only if the central velocity dispersion is derived with the observational method. The open symbols denoting the observational values in the x- and y-direction are clearly above the ‘real’ central value. Third: Simulation of a very massive satellite which shows no clear enhancement in both methods.

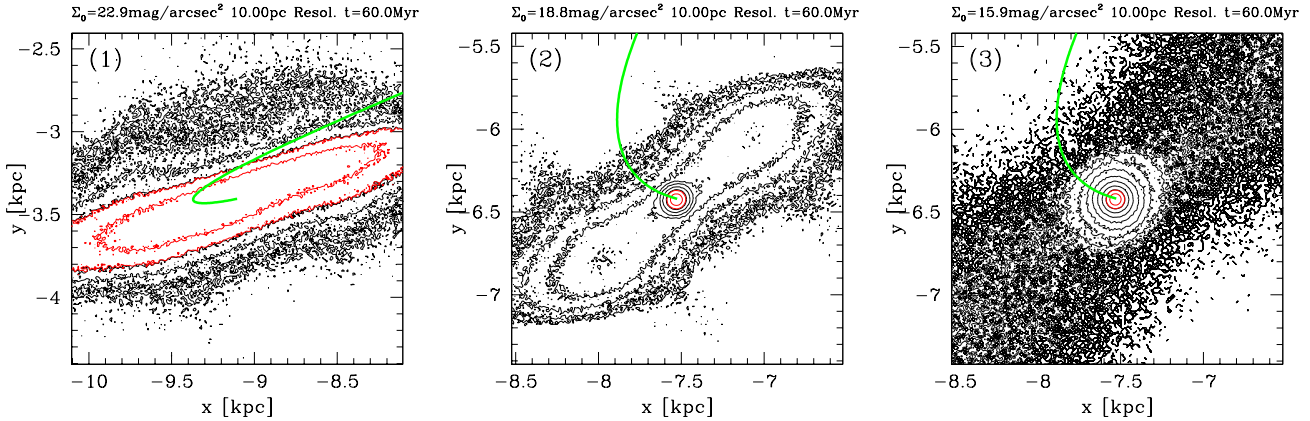


Figure 4. Contour plots of the three models of Fig. 3 in the orbital plane (x - y -plane). The centre of the host galaxy is at 0–0 kpc. The orbit of the object is plotted as the thick (online: green) line. Contours have magnitudo spacing (assumed $M = L = 1:0 M / L$) and the outermost contour corresponds to 28 mag arcsec⁻² (the two brightest contours in each panel are plotted red online). Almost filled black areas do not denote high surface brightness but areas with very faint contributions (at the given resolution the brightness fluctuates from pixel to pixel at the lowest level). First panel: This object is clearly dissolved; it shows no core anymore and is out of virial equilibrium. Second: Surviving object which shows faint tidal tails along the orbit which enhance the measured velocity dispersion. Third: This object shows only a few stars which are unbound and spread (black areas). The small fraction of these stars are not able to enhance the velocity dispersion.

show clearly that either the satellite gets completely dissolved if D_{min} is closer than 50–100 pc or shows no deviation in M/M at all (Fig. 2).

In Fig. 2 we distinguish the models according to their survival of the passage and if they show enhanced M/M -ratios. The panels show clearly that only dissolved or almost dissolved objects show enhanced M/M -ratios. All surviving objects show no deviation from virial equilibrium.

3.2 The ‘observational’ method

The results in Sect. 3.1 are based on the exact knowledge of the theoretical central line-of-sight velocity dispersion. Observers on the other hand do not have this information. The usual way to de-

termine the velocity dispersion of a marginally resolved object is to place a slit on the object and obtain a spectrum. From this spectral information one chooses one or two spectral lines and fits a template spectrum convolved with the instrumental line-width function and a Gaussian velocity distribution. This Gaussian velocity distribution measures the line-of-sight velocity dispersion of the whole object. Based on assumed theoretical models this value is then corrected to the central line-of-sight velocity dispersion. In the case of the simple Plummer model one has to multiply the result for the whole object by a factor of 1.25. Thus, the central velocity dispersion is

$$\sigma_{0;P} = \frac{r}{64R_{p1}} \sqrt{\frac{3GM_{p1}}{r}}; \quad (12)$$

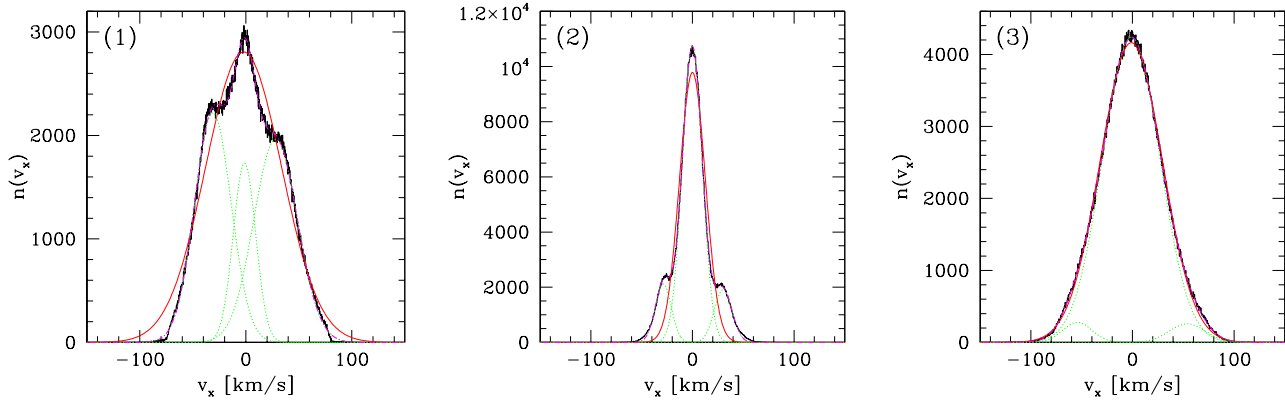


Figure 5. Same simulations as in Fig. 3. The plots show the velocity distributions along the x-axis. Histogram (online: black) are the data-points. Solid line (online: red) is the single Gaussian fit, dotted lines (online: green) are the three Gaussians to correct for fast and slow unbound particles in front and behind the object and the dashed line (online: magenta) is the sum of these three Gaussians, which is an excellent reproduction of the data and is barely visible by being masked by the data. The three Gaussians always fit the data best. While in the first panel the object is almost dissolved and the Gaussians of the unbound particles are stronger than the bound one (resulting in a M/M-ratio of 20 in x and 5 in y-direction), the second panel shows a bound object with enhanced M/M-ratio due to the small contribution of the unbound particles (M/M-ratio is 2.5 and 2.2). In the last panel the contribution of the unbound particles is too low to enhance the M/M-ratio (M/M = 1.2 in both directions and within the uncertainties of the measurement).

while the projected velocity dispersion integrated over the whole Plummer sphere is

$$\begin{aligned} \sigma_{obs,p}^{pl} &= \frac{1}{M_{pl}} \int_{-Z_1}^{Z_1} \int_0^{r_0} \int_0^{r_0} \rho(r^0) p(r^0) dr^0; \\ &= \frac{3}{100} \frac{GM_{pl}}{R_{pl}}; \end{aligned} \quad (13)$$

so that

$$\frac{\sigma_{0,p}^{pl}}{\sigma_{obs,p}^{pl}} = 1.25; \quad (14)$$

$\sigma_{0,p}^{pl}$ denotes the central line-of-sight velocity dispersion and $\sigma_{obs,p}^{pl}$ the weighted line-of-sight velocity dispersion integrated over the whole object.

As one can see in Fig. 3 it can be a crucial point how strongly a measurement of the line-of-sight velocity dispersion is contaminated by unbound stars. The observational values can highly overestimate the real central value. Unbound stars have a different velocity distribution than the bound ones. They are either travelling in front or behind the object (seen along the trajectory; this is shown in Fig. 4) and are faster or slower. But the velocity distribution of these stars which are still located in the vicinity of the object and stem from one central passage, peak on either side of the Gaussian distribution of the bound stars, leading to an effective broadening of the measured velocity distribution. Fitting just a single Gaussian will therefore lead to an enhanced measured velocity dispersion and an overestimation of the central velocity dispersion value of the satellite. This is demonstrated in Fig. 5 where the velocity distribution of all stars is shown together with the best fitting single Gaussian and the fitting curve of a triple Gaussian which takes the unbound stars into account. The measured values for the central line-of-sight velocity dispersion are shown in Table 3.

Clearly this effect is strongest in the plane of the orbit and is not visible perpendicular to it. This can be seen in Fig. 3 where the symbol for the z-axis-value in all three panels shows the same value as the direct measurement. Actually for strongly disturbed systems (i.e. high mass-loss) the values in the z-direction are below

Table 3. Central velocity dispersion along the x-axis derived by different methods. Shown are the values of the same three simulations plotted in Figs. 3 to 5 now labelled 'dissolved', 'enhanced' and 'massive', respectively. The rows show the different values of the central velocity dispersion. First row is the direct measurement of the central dispersion, 'single' denotes the central dispersion derived from the fit of a single Gaussian to the data and 'triple (c)' denotes the value of a fit using three Gaussians where the central one (c) is used to compute the velocity dispersion of the bound object.

	[km/s]	dissolved	enhanced	massive		
true actual	10:6	3:1	9:49	0:05	35:7	0:2
single	44:6	0:3	15:90	0:30	38:4	0:1
triple (c)	13:3	0:1	12:35	0:04	35:3	0:3

the line because we do not account for the change of the constant A which should increase for lower masses. But in any random orientation of the object with respect to the observer the effect of the enhanced M/M-ratio should at least be partly visible.

Summing up our results we state the following: Satellites which are out of virial equilibrium, i.e. in the state of dissolution show enhanced virial masses and therefore the real mass content is overestimated. Figure 6 shows in the first panel the M/M-ratio plotted against the ratio of final to initial bound mass of the object. The dividing dashed line separates objects which have lost more than 50 per cent of their mass during the central passage and are already dissolved or are not likely to survive the next passage, from objects which are stable for several more passages through the centre. While on the left side the derived M/M-ratios (using the observational method) can climb up to very high values, the stable objects show only slight enhancements of the ratio if at all. But in the second panel one already sees that even if the object itself is in virial equilibrium ($M_{vir} = M_b = 1.0$) there are satellites which show a broadening of the velocity distribution leading to an enhanced mass-ratio if measured the observational way. The third panel finally shows an enlargement of this area and one finds M/M-ratios overestimated by up to a factor of five. Surviving ob-

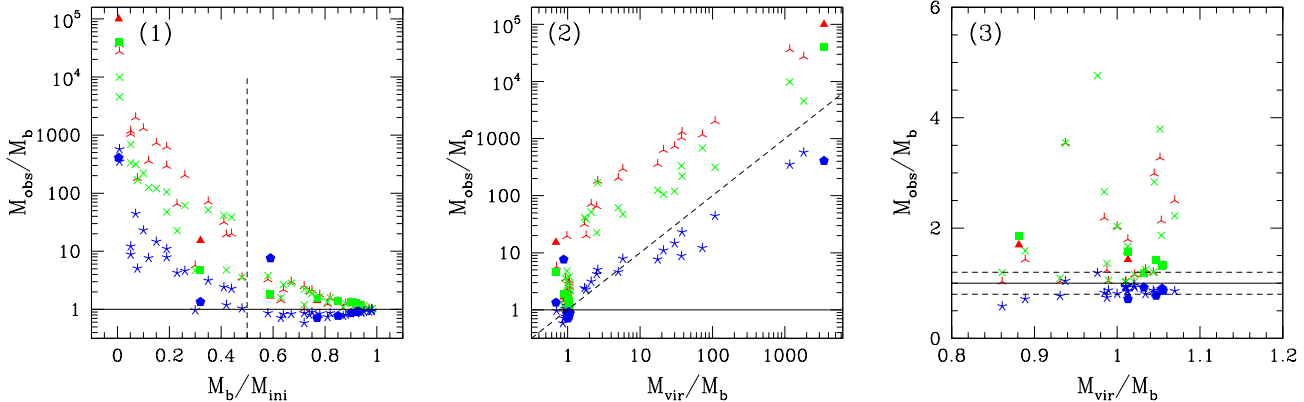


Figure 6. Summary of the results derived using the observational method (Sect. 3.2). M_{obs} denotes the virial mass derived by the observational method, i.e. fitting a single Gaussian to the velocity distribution, M_b denotes the real bound mass of the object, M_{ini} is the initial bound mass and M_{vir} is the virial mass derived by the analytical method (Sect. 3.1). Measurements along the x-axis are three-pointed stars (online: red), along the y-axis are crosses (online: green) and z-axis measurements are represented by five-pointed stars (online: blue). Simulations with initial parameters similar to the UCDs in Virgo are represented by filled symbols. First panel shows the derived mass-ratio as a function of the final/initial bound-mass-ratio. Satellites with final masses larger than 50 per cent of the initial mass (right of the dashed line) are deemed stable against immediate tidal destruction. Objects left of the dividing line are out of equilibrium and therefore have to show enhanced M/M -ratios. But there are also data points which are larger than one on the right of the dividing line. Second panel shows the same results but now the observational M/M -ratio is plotted against the analytical ratio. All data-points except the measurements perpendicular to the orbit are above the ‘analytical’ method (dashed line shows the line where the values of the observational method are equal to the direct method). z-values are below the dashed line because we do not correct the constant A for objects with high mass-loss. A clump of data-points is visible around $M_{\text{vir}}/M_b = 1$ which points to overestimated masses. The third panel finally is a magnification of this region. One clearly sees that the observational method can lead to overestimates of the true mass by a factor of up to five. Horizontal line shows a ratio of 1 with dashed lines denoting an error range of 20 per cent.

jects which show an enhancement in their M/M -ratio, if measured with this observational method, are already marked in Fig. 2 with a small ‘e’. As one can see there is a range of critical distances ($D > 100$ pc and $D < 1$ kpc) to the centre of the host galaxy where an UCD like the ones found in Virgo could show an overestimated mass-to-light ratio.

3.3 Observability

In the previous section we claimed that with the ‘observational’ method the mass-to-light ratios of UCDs could be overestimated, because the velocity distribution is not Gaussian any more but ‘contaminated’ by unbound stars around the object. In this section we show that there is almost no chance for an observer to detect this ‘non-Gaussianity’ of the velocity distribution.

When measuring a spectrum of a distant object, observers have to deal with two major shortcomings. First there is the intrinsic line-width produced mainly by the instrument. State-of-the-art instruments like UVES or Flames can reduce this line-width down to about 2 km s^{-1} . But the observations of the UCDs in Virgo were made with an instrumental line-width of about 25 km s^{-1} .

The second effect an observer has to take into account is noise in the spectrum.

Taking the velocity distribution from the enhanced M/M -ratio simulation we fold it with a Gaussian of the width σ_i to mimic the instrumental line-width and determine at which line-width the ‘features’ of our distribution are washed out. This happens at an instrumental line-width of $\sigma_i = 7.5 \text{ km s}^{-1}$ (as shown in Fig. 7). Then we take the best state-of-the-art line-width of $\sigma_i = 2 \text{ km s}^{-1}$ and add random white noise to the distribution until again the ‘features’ are almost invisible again. This happens already at a signal-to-noise ratio of 20 (see Fig. 7 lower left panel). In the final panel of Fig. 7

we fold our distribution with the line-width of the observations of the Virgo-UCDs and add noise to mimic the same S/N-ratio as in the observations. There is no deviation from Gaussianity visible any more.

4 DISCUSSION & CONCLUSION

We have shown with our models that dwarf satellites around a giant elliptical galaxy like M87 can have an enhanced mass-to-light ratio due to close passages to the centre of the host galaxy. While very close passages lead to the destruction of the satellite there are orbits which allow for enough ‘damage’ to the satellite to enhance the mass-ratio (measured the same way an observer would do) without completely destroying the object.

The amount of destruction is larger if the satellite is less massive and less concentrated. But the loss of about 20 per cent of the initial mass is enough to have the object surviving several more close passages and to mimic an enhanced mass-to-light ratio. For models comparable to the UCDs in Virgo and Fornax the range of possible minimum distances during central passages is about 100 to 1000 pc. All passages closer to the centre lead to complete destruction and all passages further away show no measurable effect at all, except for a mass-loss of the order of a few per cent. We therefore conclude that the enhanced M/L -ratios measured for the Virgo UCDs by Hasegan et al. (2005) may not be due to dark matter.

A more general result of our study is the discrepancy between the derived virial masses if one has access to the correct properties of the satellites compared to the virial masses derived the way an observer would measure. While very massive objects which are almost unaffected by tidal forces show the same results within the uncertainties one has to be careful if objects are less massive and are surrounded by a cloud of tidally stripped stars. These stars are

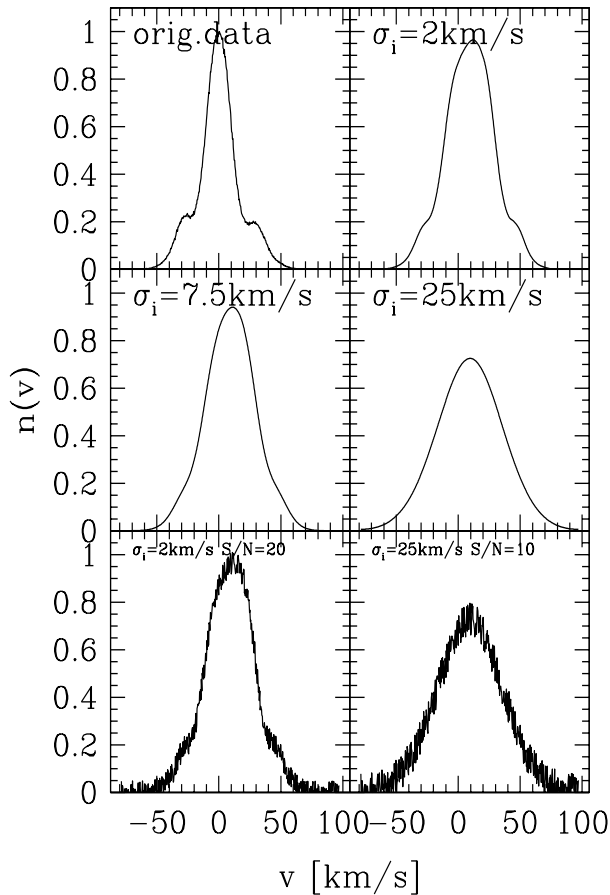


Figure 7. The top left panel shows the original velocity distribution. At the top-right panel this distribution was folded with a Gaussian of the width 2 km s^{-1} which mimics the best intrinsic instrumental line-width available today. The middle panels show the same distribution but folded with a Gaussian of the width 7.5 km s^{-1} (left) and 25 km s^{-1} (right). The left panel shows the transition when the non-Gaussian features of the original distribution start to disappear. In the bottom panels we also added white noise to the folded distribution to mimic the noise an observer has in the spectrum. At the left panel we took the folded distribution with the best available line-width again and added noise to reach a S/N of 20. This is again the transition where the features start to disappear. With more noise the features are not visible any more. Clearly with higher intrinsic line-widths the features disappear at lower noise-levels. The right panel mimics the properties of the spectra of the UCDs in Virgo (Hasegan et al. 2005). There the intrinsic line-width was 25 km s^{-1} and the S/N-ratio was 10.

either faster or slower in the mean but their mean values are not too different to the bulk velocity of the bound stars to clearly disentangle the 'populations' (populations in the sense of within, in front or behind the object). Especially if the broadening of a spectral line is estimated by fitting the template line folded with a Gaussian for the instrumental line-width and a single Gaussian for the velocity distribution can the deduced central velocity dispersion be too high thus leading to a mass-to-light ratio that is too large by up to a factor of ten.

Effects like this have to be given serious consideration when

measuring velocity dispersions of faint and distant objects.

Acknowledgements:

MF thankfully announces financial support through DFG-grant KR1635/5-1 and PPARC. We also want to thank M. Hilker and T. Richtler for useful comments regarding how to mimic observations.

REFERENCES

- Aarseth S.J., Hénon M., Wielen R., 1974, *A&A*, 37, 183
 Bekki K., Couch W.J., Drinkwater M.J., 2001, *ApJ*, 552, 105L
 Bekki K., Couch W.J., Drinkwater M.J., Shioya Y., 2003, *MNRAS*, 344, 399
 Chandrasekhar S., 1943, *ApJ*, 97, 255
 De Propriis R., Phillipps S., Drinkwater M.J., Gregg M.D., Jones J.B., Evstigneeva E., Bekki K., 2005, *ApJ*, 623, 105L
 Di Matteo T., Allen S.W., Fabian A.C., Wilson A.S., Young A.J., 2003, *ApJ*, 582, 133
 Dirsch B., Richtler T., Geisler D., Forte J.C., Bassino L.P., Gieren W.P., 2003, *AJ*, 125, 1908
 Evstigneeva E.A., Gregg M.D., Drinkwater M.J., 2005, to appear in the proceedings of IAU Colloquium 198, astro-ph/0504289
 Fellhauer M., Kroupa P., 2002, *MNRAS*, 330, 642
 Fellhauer M., Kroupa P., 2005, *MNRAS*, 359, 223
 Fellhauer M., Kroupa P., Baumgardt H., Bien R., Boily C.M., Spurzem R., Wassmer N., 2000, *NewA*, 5, 305
 Hasegan M., Jordan A., Cote P., Djorgovski S.G., McLaughlin D.E., Blakeslee J.P., Mei S., West M.J., Peng E.W., Ferrarese L., Milosavljevic M., Tonry J.L., Merrit D., 2005, *ApJ*, 627, 203
 Hilker M., 1998, PhD-thesis, University of Bonn
 Hilker M., Infante L., Richtler T., 1999, *A&AS*, 138, 55
 King I., 1966, *AJ*, 71, 61
 Kroupa P., 1997, *NewA*, 2, 139
 Kroupa P., 1998, *MNRAS*, 300, 200
 Maraston C., Bastian N., Saglia R.P., Kissler-Patig M., Schweizer F., Goudfrooij P., 2004, *A&A*, 416, 467
 Mayer L., Governato F., Colpi M., Moore B., Quinn T., Wadsley J., Stadel J., Lake G., 2001, *ApJ*, 559, 754
 Mayer L., Moore B., Quinn T., Governato F., Stadel J., 2002, *MNRAS*, 336, 119
 McLaughlin D.E., 1999, *ApJ*, 512, 9L
 Mieske S., Hilker M., Infante L., 2002, *A&A*, 383, 823
 Mieske S., Infante L., Bentez N., Coe D., Blakeslee J.P., Zekser K., Ford H.C., Broadhurst T.J., Illingworth G.D., Hartig G.F., Clampin M., Ardila D.R., Bartko F., Bouwens R.J., Brown R.A., Burrows C.J., Cheng E.S., Cross N.J.G., Feldman P.D., Franx M., Golimowski D.A., Goto T., Gronwall C., Holden B., Homerier N., Kimble, R.A., Krist J.E., Lesser M.P., Martel A.R., Menanteau F., Meurer G.R., Miley G.K., Postman M., Rosati P., Sirianni M., Sparks W.B., Tran H.D., Tsvetanov Z.I., White R.L., Zheng W., 2004, *AJ*, 128, 1529
 Phillipps S., Drinkwater M.J., Gregg M.D., Jones J.B., 2001, *ApJ*, 560, 201
 Plummer H.C., 1911, *MNRAS*, 71, 460
 Portegies Zwart S.F., McMillan S.L.W., 2002, *ApJ*, 576, 899
 Vesperini E., Zepf S.E., Kundu A., Ashman K.M., 2003, *ApJ*, 593, 760